



1 Article

Holographic fabrication and optical property of

graded photonic super-crystals with a rectangular

4 unit super-cell

- 5 Safaa Hassan 1, Oliver Sale 1, David Lowell 1, Noah Hurley 1, and Yuankun Lin 1.2,*
 - ¹ Department of Physics, University of North Texas, Denton, TX 76203, USA; SafaaHassan@my.unt.edu (S.H.); OliverSale@my.unt.edu (O.S.); DavidLowell@my.unt.edu (D.L.); NoahHurley@my.unt.edu (N.H.).
 - ² Department of Electrical Engineering, University of North Texas, Denton, TX 76203, USA
- 9 * Correspondence: yuankun.lin@unt.edu; Tel.: +1-940-565-4548

10 11

12

13

14

15

16

17

18

19

20

21

22

23

6

7

8

Received: date; Accepted: date; Published: date

Abstract: The recently <u>developed</u> graded photonic super-crystals show an enhanced light absorption and light extraction efficiency if they are integrated with a solar cell and an organic light emitting device, respectively. In this paper, we present the holographic fabrication of graded photonic super-crystal with a rectangular unit super-cell. Spatial light modulator based pixel-by-pixel phase engineering of incident laser beam provides a high resolution phase pattern for interference lithography. This also provides a flexible design for graded photonic super-crystals with a different ratio of length over width for the rectangular unit super-cell. The light extraction efficiency is simulated for the organic light emitting device where the cathode is patterned with the graded photonic super-crystal. The high extraction efficiency is maintained for different exposure thresholds during the interference lithography. Desired polarization effects are observed for certain exposure thresholds. The extraction efficiency reaches as high as 75% in the glass substrate.

Keywords: photonic crystals; graded photonic super-crystals; holographic lithography; extraction efficiency; organic light emitting device; spatial light modulator.

24 25

26

27

28

29

30

31

32

33

34

35

36

37

38

39

40

41

42

1. Introduction

Photonic crystals have been extensively studied for the integration of functional optical devices, photonic band gap engineering, and enhanced light-matter interaction [1-3]. Traditional twodimensional (2D) photonic crystals [4] have uniform lattices as shown inside the solid green rectangle in Fig. 1. The second generation 2D photonic crystals [5-6] have dual lattices with one set of lattices indicated by the blue dots and the other by the red dots in Fig. 1. The second generation photonic crystals have shown enhanced light-matter interaction [5-6]. Very recently, we have studied a new type of photonic crystals: titled graded photonic super-crystals (GPSC) [7-11]. Although the lattices are grouped by the blue and red dots, the size of basis is different in GPSC. The basis size is gradient becoming smaller along the arrows for both blue and red lattice sets in Fig. 1 then becoming larger after a quarter of period. The unit cell becomes unit super-cell in the GPSC as opposed to the dual lattice in the second-generation photonic crystals. "Period 1" is the period for the traditional photonic crystal while "Period 2" is the second period in the x-direction for the GPSC as shown in Fig. 1. The lattice described by "Period 1" have a square symmetry while the lattice described by "period 2" can have square, hexagonal or five-fold symmetry [7-11]. Thus, the GPSC can have dual-periods and dual-symmetries. The lattice with "Period 1" can have other symmetries with a cost of reduced resolution in a phase pattern if a spatial light modulator (SLM) is used in the fabrication [7-11]. The

filling fraction of dielectric material in the GPSC is also gradient for regions where the dashed green rectangular region has a high filling fraction and the solid green rectangular region has a low filling fraction.

Multiple-beam based interference lithography has been used for the fabrication of a photonic crystal template [12-19]. The use of a phase mask or single reflection optical element has greatly reduced complexity and improved the mechanical stability of the optical setup [13-19]. Recently SLM has been used as an electrically adjustable phase mask for the interference lithography [20-27]. The computer-generated hologram method can be used for the fabrication of the desired structure using the SLM. However, pixel-by-pixel phase engineering in the SLM can reach a high resolution in holographic fabrication [7,10,11,26,27]. Another advantage of using pixel-by-pixel phase engineering is that a Fourier filter can be predicted, and an aforementioned reflective optical element can be integrated for large area holographic fabrication [10]. Using the pixel-by-pixel phase engineering method, graded photonic super-crystals with square [7], hexagonal [7] and five-fold symmetric [11] unit super-cells have been fabricated. These four, five and six-fold structures were formed by four outer beams with large interfering angles plus four, five or six inner beams with small interfering angles, respectively [7,11]. The interfering angles of these four common outer beams can be increased using single reflective optical element for the formation of graded photonic super-crystals with a small "Period 1" [10]. Rectangular structures is less symmetric than the four, five and six-fold structure. It is interesting to know whether there is a polarization effect and whether the light extraction can be improved or reduced if the cathode of organic light emitting device is patterned with less symmetric graded photonic super-crystals.

In this paper, we study the holographic fabrication of graded photonic super-crystals with a rectangular unit super-cell. A rectangular unit super-cell in phase pattern is designed to have a desired ratio of length over width. We also study the extraction efficiency and polarization effect of the light from the organic light emitting device where the cathode is patterned with the graded photonic super-crystal. An extraction efficiency of up to 75% can be reached in the simulation.

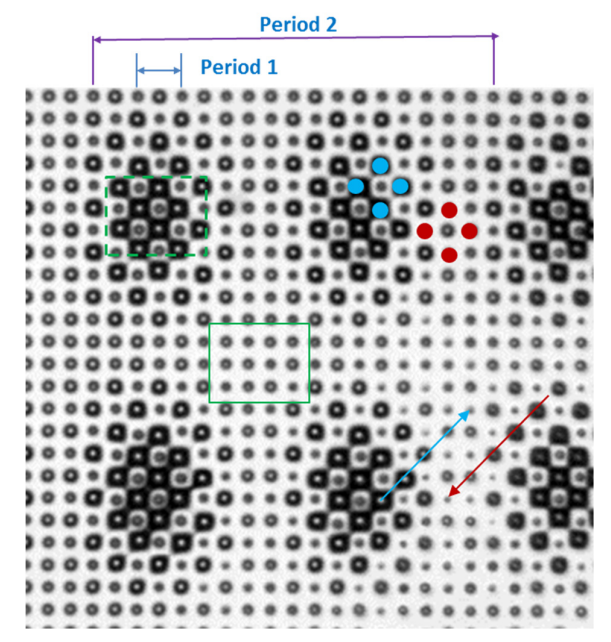


Figure 1. Image of a graded photonic super-crystals: the lattices can be grouped by blue and red dots. The size of the basis becomes smaller along the blue and red arrows then becomes larger after a quarter of period 2). The filling fraction of dielectric material is higher inside the dashed green rectangle than the solid green rectangle. The graded photonic super-crystals have a unit super-cell as indicated by "period 2" in x-direction.

A 532 nm laser beam (Cobolt Samba 50 mW) was expanded and collimated using lens and a spatial filter. The phase of the laser beam was modulated by the engineered phase pattern displayed in a phase-only SLM (Holoeye PLUTO). It has an active area of 15.36×8.64 mm² with a 1920×1080 pixels. The pixel size of the SLM is $8 \times 8 \mu m^2$ (P=side length of pixel square= $8 \mu m$ is used in this paper). The laser is linearly polarized along the longer side of the active area and is incident onto the SLM with an incident angle of 4 degrees relative to the normal to the SLM. As shown in Fig. 2(a), the diffracted beams from the phase pattern, Fig. 2(b), displayed in the SLM are collected through lens1 and selected by a Fourier filter at the Fourier plane.

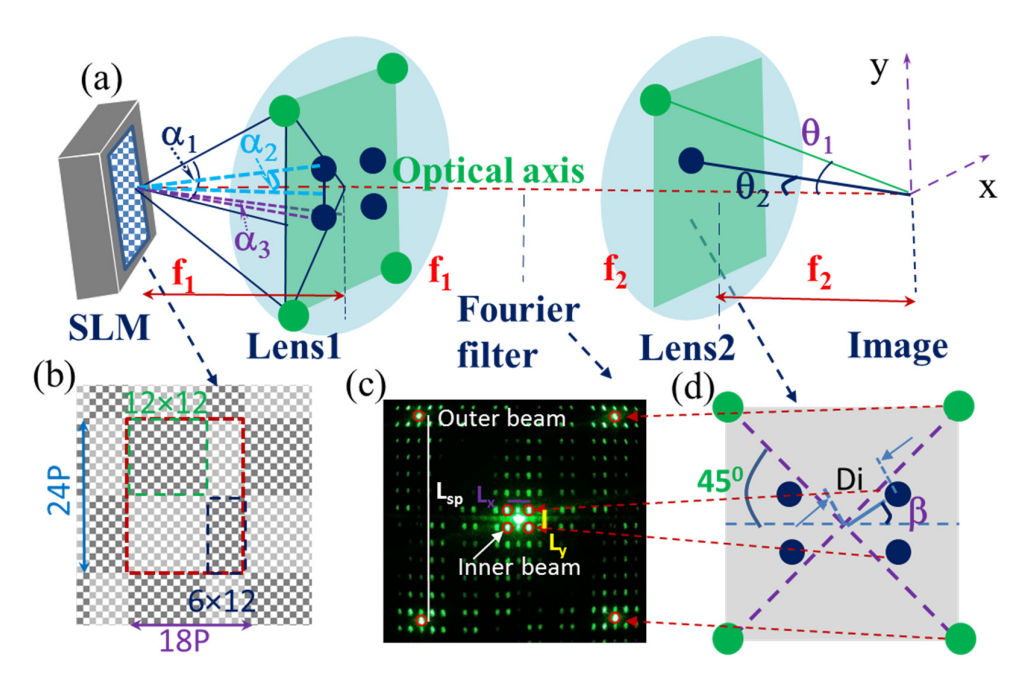


Figure 2. (a) Schematic of the optical setup for the holographic fabrication. The SLM is used to display phase patterns. The diffracted beams from the SLM are filtered at the Fourier Plane and form interference patterns through 4f imaging system of lens 1 and lens 2. α_1 , α_2 , α_3 are the first order diffraction angles due to the periodic array of 2P pixels in x and y directions, 24P pixels in y direction and 18P pixels in x-direction in the phase pattern in (b), respectively. θ_1 and θ_2 (zenith angle) are the interfering angles of outer beam and inner beams in (c), respectively. (b) An enlarged view of designed phase patterns. A unit super-cell is indicated by the dashed red square. Inside the unit-cell, there are two 12×12 square pixel patterns and two 12×6 square pixel patterns. The gray levels of (190, 254) correspond to the dashed green and blue regions while (128, 254) correspond to the remaining regions inside the unit super-cell. (c) The laser diffraction pattern from the phase pattern in (b) at the Fourier plan. A Fourier filter is used to allow the diffraction spots inside the red circles passing through. (d) Schematic of eight beams corresponding to the outer and inner beams in (c) for the interference lithography. β is an azimuthal angle for one of inner beams in (c).

A unit super-cell of the phase pattern is indicated by a dashed red square in Fig. 2(b). The unit super-cell was divided into two 12×12 checkerboard regions and two 12×6 checkerboard regions. The gray levels of (190,254) are used for the regions inside dashed green and blue squares while (128,254) are used for the regions outside dashed green and blue squares in the unit super-cell. The gray levels were selected based on the diffraction efficiency of a small-period pattern verses a large-period pattern, their ratio, and the formation of a graded photonic super-crystals through simulation [7,11]. A simulation of an interference pattern of multi-beams with measured diffraction efficiencies and a certain exposure threshold was used to determine the gray level selection [11]. A gamma curve modulated a 0π and 2π phase into the laser beam when it as reflected by a gray level of 0 and 255, respectively, and related the phase and gray level almost linearly between 0 and 255. A gray level of

113 190 corresponds to a phase of $(190 \times 2\pi/255)$. A gray level of 254 was typically used instead of 255 because 255 corresponds to 2π or 0π in the cosine function in the simulation.

When the 532 nm laser is incident onto the phase pattern in the SLM, it is diffracted following the equation (1):

$$D \times \sin \alpha_i = n\lambda, \qquad i = 1, 2, 3$$
 (1)

Where D is the structural period, α the first order diffraction angle as defined in Fig. 2(a) and described below, and n the diffraction order. α_1 is the first order diffraction angle due to the periodic array of the gray levels of (128, 254) or (190, 254) and can be obtained by setting D=2P in Eq. (1). For a large period in x- and y-directions, D in Eq. (1) equals 18P and 24P, and α_1 equals α_2 and α_2 , respectively. The distance L_{sp}, L_x, L_y between the +1 and -1 order diffractions due to small period (SP) 2P arrays, 18P arrays in x-direction and 24P arrays in y-direction can be measured in Fig. 2, respectively. The diffraction condition in Eq. (1) was tested by verifying that L_{sp}=2×f₁ tan(α_1), L_x=2×f₁ tan(α_2) as shown in Fig. 2(a) and 2(c). Theoretically L_{sp}/L_x=9 and L_{sp}/L_y=12. As measured in Fig. 2(c), L_{sp}/L_x=9.20 and L_{sp}/L_y=12.23. The agreement between the measured and theoretical values is high, indicating the correct assignment for D.

In the experimental setup, lenses with focal lengths of f1=400 mm and f2= 200 mm for lens 1 and lens 2, respectively, were used. 4f setup as shown in Fig. 2(a) was used. The graded photonic supercrystal was fabricated by exposing the dipentaerythritol penta/hexaacrylate (DPHPA) mixture to the inference pattern with similar spin-coating, exposure, and development conditions as in reference [7,10,11].

3. Results

3.1 Holographic fabrication results

The red circles in Fig. 2(c) are the Fourier filter that is used to allow these eight beams pass through. These eight beams are represented by the following equations:

$$\mathbf{E}_{1}(r,t) = \mathbf{E}_{1}\cos[+(k \sin\theta_{1} \cos 45)x + (k \sin\theta_{1} \sin 45)y + (k \cos\theta_{1})z - \omega t + \phi_{1}] \tag{2}$$

$$\mathbf{E}_{2}(r,t) = \mathbf{E}_{2}\cos[-(k \sin\theta_{1} \cos 45)x + (k \sin\theta_{1} \sin 45)y + (k \cos\theta_{1})z - \omega t + \phi_{2}] \tag{3}$$

$$\mathbf{E}_{3}(r,t) = \mathbf{E}_{3}\cos[-(k \sin\theta_{1} \cos 45)x - (k \sin\theta_{1} \sin 45)y + (k \cos\theta_{1})z - \omega t + \phi_{3}] \tag{4}$$

$$\mathbf{E}_{4}(r,t) = \mathbf{E}_{4}\cos[+(k \sin\theta_{1} \cos 45)x - (k \sin\theta_{1} \sin 45)y + (k \cos\theta_{1})z - \omega t + \phi_{4}] \tag{5}$$

$$\mathbf{E}_{5}(r,t) = \mathbf{E}_{5}\cos[+(k\sin\theta_{2}\cos\beta)x + (k\sin\theta_{2}\sin\beta)y + (k\cos\theta_{2})z - \omega t + \phi_{5}] \tag{6}$$

$$\mathbf{E}_{6}(r,t) = \mathbf{E}_{6}\cos[-(k\sin\theta_{2}\cos\beta)x + (k\sin\theta_{2}\sin\beta)y + (k\cos\theta_{2})z - \omega t + \phi_{6}] \tag{7}$$

$$\mathbf{E}_{7}(r,t) = \mathbf{E}_{7}\cos[-(k\sin\theta_{2}\cos\beta)x - (k\sin\theta_{2}\sin\beta)y + (k\cos\theta_{2})z - \omega t + \phi_{7}] \tag{8}$$

$$\mathbf{E}_{8}(r,t) = \mathbf{E}_{8}\cos[+(k\sin\theta_{2}\cos\beta)x - (k\sin\theta_{2}\sin\beta)y + (k\cos\theta_{2})z - \omega t + \phi_{8}] \tag{9}$$

where E is the electric field, k is the wave vector, θ_1 and θ_2 (zenith angle) are the interfering angles of outer beam and inner beams in Fig. 2, respectively, 45° and β are the azimuthal angles for outer and inner beams in Fig. 2, respectively, and ϕ is the initial phase of the beam. When the eight beams are overlapped, the intensity distribution in the interference pattern is determined by

$$I(r) = \langle \sum_{i=1}^{8} E_i^2(r,t) \rangle + \sum_{i < j}^{8} \mathbf{E}_i \cdot \mathbf{E}_j \cos[(k_j - k_i) \cdot r + (\phi_j - \phi_i)].$$
 (10)

The nine equations (2-10) were programed in Matlab that produced interference patterns with one example in Fig. 3(a). The eight-beam interference can also be approximately understood by adding the interference of beams 1-4 and beams 5-8. The inference of beams 1-4 forms a structure with a small period Λ_s =2 π /(k sin(θ_1) cos(45)) where θ_1 is determined by tan(θ_1)= f_1 tan (α_1)× $\sqrt{2}/f_2$. Thus, Λ_s =(f_2/f_1) 2P. The period Λ_x in x-direction in the interference among beams 5-8 is different from the period Λ_y in y-direction and they are calculated as follows: Λ_x =2 π /(k sin(θ_2) cos(θ_1) and θ_2 0 cos(θ_3) where sin(θ_2) cos(θ_3) cos(θ_3) and sin(θ_2) sin(θ_3) sin(θ_3) cos(θ_3) as shown in Fig. 2(c) and 2(d). Thus, Λ_x =(f_2/f_1) 18P and Λ_y =(f_2/f_1) 24P.

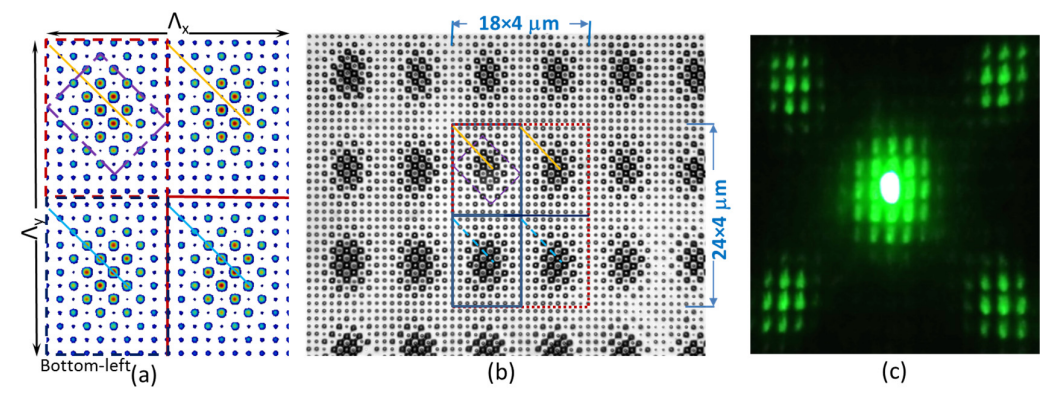


Figure 3. (a) Simulated eight-beam interference pattern. (b) <u>CCD</u> (attached to an optical microscope) image of the fabricated graded photonic super-crystal in DPHPA. (c) Diffraction pattern of a fabricated sample from 532 nm laser.

A simulated eight-beam interference pattern as shown in Fig. 3(a) assumes the same initial phase for all eight beams in Eq. (10). The periodicity in the x- and y-directions (Λ_x , Λ_y) is labeled for the size of the unit super-cell in the holographic structure in Fig. 3(a). Although both the square (12×12) and rectangular (6×12) sub-unit cells are used in Fig. 2(b), the sub-unit cell, as indicated by the dashed red line, is in a rectangular shape in Fig. 3(a). The unit super-cell in Fig. 3(a) has a ratio of length over width of Λ_y/Λ_x =24/18, which is obtained from (12+12)/(12+6) in Fig. 2(b). The design of the phase pattern is flexible for obtaining a rectangular unit super-cell in holographic structure. For example, the unit super-cell in phase pattern can have a sub-unit of k×k and k×m pixels. The obtained holographic structure can have a rectangular unit super-cell with a ratio of side lengths defined by 2k/(k+m).

Fig. 3(b) shows a CCD (attached to the optical microscope) image of the fabricated graded photonic super-crystals in DPHPA. The graded pattern and dual periodicity (one in 4 μ m and others in 18×4 μ m and 24×4 μ m) are clearly demonstrated in Fig. 3(b). The fabricated pattern has a unit supercell indicated by a dashed red rectangle with a size of (18×4 μ m) times (24×4 μ m). The super-cell can be divided into four sub-units dictated by the blue square in Fig. 3(b), which corresponds to the sub-unit dictated by the dashed red rectangle in simulation in Fig. 3(a). The lattice has a small period of 4 μ m for both x and y-directions. The graded lattice clusters have a rectangular symmetry. Thus, we have a graded photonic super-crystal with square lattices and rectangular lattice clusters.

The diffraction pattern of the fabricated sample is shown in Fig. 3(c), using 532 nm laser. Near the 0th order diffraction spot, there are several high order diffractions. In the four corners, there are more than nine diffraction spots in each, due to the small periodic lattice and graded feature. The multiple-order diffraction indicates not only the quality of fabricated sample but also the strong lightmatter interaction which can be used for light extraction as described in next section.

177

178

179

180

181

182 183

184

185

186

187

188

189

190

191

192

193

194

195

196

197

198

199

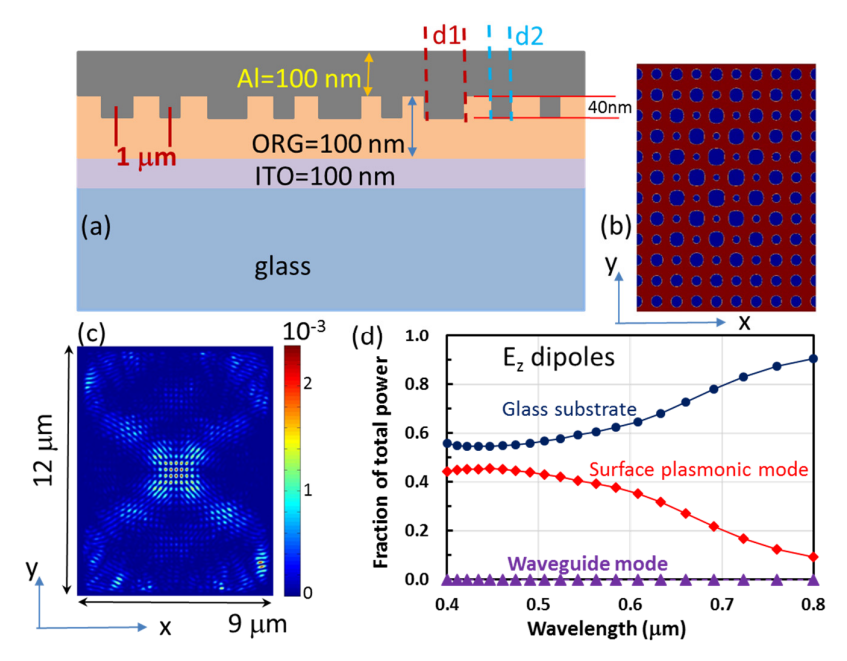


Figure 4. (a) Schematic of the organic light emitting device (OLED) where the cathode (Al) is patterned with the graded photonic super-crystal that has a rectangular unit super-cell. (b) Output of the structure design from the simulation software MEEP. (c) Electric-field intensity in the glass substrate in OLED <u>at the location 740 nm away from ITO layer</u>. (d) The fraction of the total <u>emitted</u> power in glass substrate, both in surface plasmonic mode and in waveguide

3.2 Simulation of light extraction efficiency

In this section, we simulate the light extraction efficiency in organic light emitting device (OLED), where the cathode is patterned with the graded photonic super-crystal with the rectangular unit super-cell, using the MIT Electromagnetic Equation Propagation (MEEP) simulation tool [28]. The small period of 4 µm in Fig. 3 can be reduced to a desirable value using the single reflective optical element method [10]. In this simulation, a lattice period (small period) of 1 μm is used as shown in Fig. 4(a). The 100 nm organic-layer (ORG) includes the light emitting layer, electron transport layer, and the hole transport layer. We assigned refractive indices n for the glass (n=1.45), organic (n=1.8), and ITO (n=1.8) layers [8,29]. Ten different incoherent electric point-dipole sources were placed along a vertical line in the center of ORG layer and dipoles with different polarization directions are assigned [29]. The interference pattern in Fig.3 (a) can be divided into 4 sections. Top two sections have a low-intensity lattice set starting from the top-left corner of each section, indicated by the yellow lines. The bottom two sections have a high-intensity lattice set starting from the corner as indicated by blue line. The simulation results should be the same if we select a quarter of unit super-cell or the whole one based on our experience [8,9,11]. One case for the simulation of different sections was described in Fig. 4 in reference 9. To save the computation time, a quarter of unit supercell (bottom left section in Fig. 3(a)) was used in the simulation. Fig. 4(b) shows a permittivity structure output from the MEEP tool with a sub-unit cell size of $9a \times 12a$ (a = 1000 nm)Due to the large unit super-cell (12×9 times larger than the one in traditional photonic crystal) we performed parallel simulations using the Simpetus Electromagnetic Simulation Platform in Amazon Web Services (AWS). The E-field intensity was monitored, as shown in Fig. 4(c) as an example in the glass substrate in OLED. The fraction of total power as a function of wavelength can be obtained for light in the glass substrate, light absorbed by Al cathode (in plasmonic mode), and trapped as a waveguide mode, as shown in Fig. 4(d).

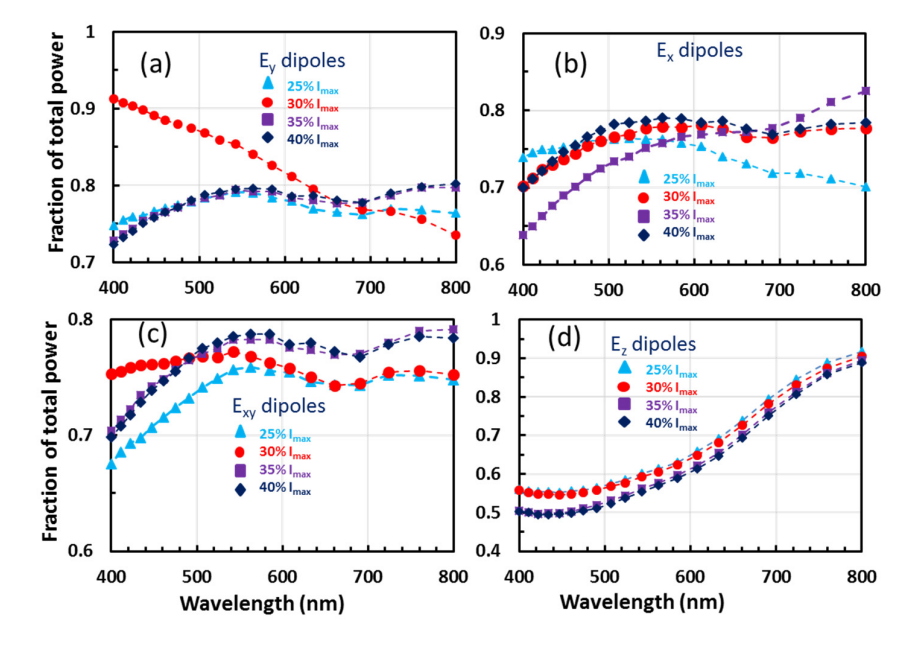


Figure 5. (a) Fraction of total <u>emitted</u> power (light in glass substrate over total <u>emitted</u> power) as a function of wavelengths for different exposure threshold of 25% I_{max}, 30% I_{max}, 35% I_{max} and 40% I_{max} for E_y dipoles (a), E_x dipoles (b), E_{xy} dipoles (c), and E_z dipoles (d)

Light intensity in air in fraction is 6.6% less than that in glass substrate as simulated for other structures [11]. However, the simulation of extraction efficiency into the glass substrate takes much less time. To save the computation times and focus on the fabrication effect, we simulate the extraction efficiency into the glass substrate for OLED where the cathode (Al) is patterned with the graded photonic super-crystal holographically formed under different exposure threshold. Figure 5 shows the percentage of light in the glass substrate over the total power as a function of wavelengths for the rectangular sub-unit as shown in Fig. 4(b). The laser exposure thresholds of 25%, 30%, 35% and 40% of the maximum intensity I_{max} are used. The results for dipole polarization of E in the v, x, xy, and z-directions are shown in Fig. 5(a,b,c,d), respectively. Overall, the extraction efficiency is between 70% and 80% for dipole polarization in xy plane except for exposure threshold of 30% Imax for E_y dipole polarization. The extraction efficiency is 86.8% for E_y dipoles for 30% I_{max} threshold while it is 76.6% for Ex dipoles at 524 nm. It is reasonable because the graded intensity is modulated in a higher number of steps along a length of the rectangle in the y-direction rather than the x-direction. If a polarization effect is needed in an OLED [30], a grade photonic super-crystal with a rectangular unit super-cell can help to reach the goal. For the laser exposure threshold of 30% Imax, the maximum extraction efficiency is at the infrared range beyond 800 nm. Further study in the discussion section will shift the wavelength for the maximum efficiency toward the visible range. The extraction efficiency for Ez dipoles in Fig. 5(d) is not significantly depended on the exposure threshold as the groove depth of 40 nm in Fig. 4(a) is fixed in the simulation. An overall light extraction efficiency p can be calculated using the average efficiency of the dipoles polarized in x-y (parallel dipole) and z (perpendicular dipole) [8,29]:

200

201

202

203

204

205

206

207

208209

210

211

212

213

214

215

216

217

218

219

220

221

222

$$\rho = \frac{2}{3}\rho_{x-y} + \frac{1}{3}\rho_z \tag{11}$$

<u>It should be noted that ρ_{x-y} and ρ_z are also the average efficiency for ten dipoles.</u> The extraction efficiency is calculated to be 71.5% at 563 nm and 73.6% at 633 nm. Under all exposure threshold conditions, the lowest overall extraction efficiency is 64.9% at 434 nm in the visible range.

4. Discussion

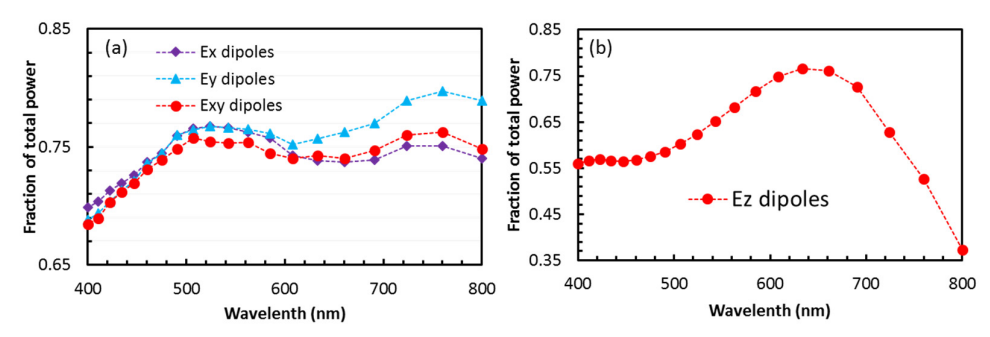


Figure 6. Fraction of total emitted power as a function of wavelengths with an exposure threshold of 35% I_{max} for E_x , E_y , and E_{xy} dipoles (a), and E_z dipoles (b) for OLED patterned with the graded photonic super-crystal with a sub-unit cell size of 9 $a \times 12$ a (a = 750 nm).

The simulation parameters used in Fig. 4 and 5 are the same as the graded photonic super-crystal with a square super-unit [8] where the maximum efficiency for the Ez dipoles occurred at 400 or 760 nm. The maximum efficiency for the Ez dipoles in Fig. 5 was in the infrared range beyond 800 nm. If we scale down the lattice period from 1000 nm to 750 nm, the wavelength for maximum efficiency is expected to be shifted from 800 to $800 \times 750/1000 = 600$ nm. Figure 6 shows simulated extraction efficiency for OLED where the cathode is patterned with a graded photonic super-crystal with a subunit cell size of 9 $a \times 12$ a (a = 750 nm) with a similar groove depth of 40 nm. There are no large differences in the extraction efficiencies for the Ex, Ey, and Exy dipoles in Fig. 6(a). As shown in Fig. 6(b), the wavelength for the maximum extraction efficiency is 633 nm, close to the expected wavelength. In the range between 608 and 690 nm, the extraction efficiency is above 75%.

The high light extraction efficiency can be understood through the effective light coupling condition provided by the graded photonic super-crystals in Eq. (12) [31]:

$$\frac{2\pi}{\lambda} n_{eff} - \frac{2\pi}{\lambda} \sin(\theta) = R \tag{12}$$

where n_{eff} is the effective refractive index of the graded photonic super-crystal, λ is the wavelength in free space, and R is the reciprocal lattice vector. The effective refractive index is related to the filling fraction f by Eq. (13):

$$n_{eff} = \sqrt{n_{metal}^2 f + n_{org}^2 (1 - f)} \tag{13}$$

where n_{metal} and n_{org} are the refractive index of the metal and organic material in the graded photonic super-crystal, respectively. Due to the graded filling fraction in the graded photonic super-crystal, the coupling condition can be met by many wavelength simultaneously.

The wavelength-dependent plasmonic loss is related to the size of basis at the lattice of graded photonic super-crystal [32]. When the sizes of basis at neighboring lattices are different as shown in Fig. 4(a) (d1 and d2), the plasmonic resonance condition is destroyed thus less plasmonic loss was seen in the simulation.

5. Conclusions

A graded photonic super-crystal with a rectangular unit super-cell has been holographically fabricated through pixel-by-pixel phase engineering of a laser beam in SLM. The design of the phase pattern in the SLM has shown a capability to fabricate the graded photonic super-cell with a desired ratio of length over width in the rectangular unit super-cell. A light extraction efficiency of up to 75% has been predicted in simulations from the OLED where the cathode is patterned with the graded photonic super-cell. A good extraction efficiency tolerance to the holographic fabrication has been predicted for OLED devices.

- Acknowledgments: This work is supported by research grants from the U.S. National Science Foundation under
 Grant No. CMMI- 1661842.
- Author Contributions: S.H., N.H., and D.L. performed the simulations; O.S., D.L. and N.H. performed the holographic fabrication; S.H. and D.L. contributed parallel computation tools; Y.L. analyzed data; Y.L., S. H. and O.S. wrote the paper. All authors read and commented on the manuscript.
 - Conflicts of Interest: The authors declare no conflict of interest. The founding sponsors had no role in the design of the study; in the collection, analyses, or interpretation of data; in the writing of the manuscript, and in the decision to publish the results.

References

- 1. Tandaechanurat, A.; Ishida, S.; Guimard, D.; Nomura, M.; Iwamoto, S.; Arakawa, Y. Lasing oscillation in a three-dimensional photonic crystal nanocavity with a complete bandgap. Nat. Photonics **2011**, 5, 91–94.
- 2. Ergin, T.; Stenger, N.; Brenner, P.; Pendry, J.B.; Wegener, M. Three-dimensional invisibility cloak at optical wavelengths. Science **2010**, 328, 337–339.
 - 3. Qi, M.; Lidorikis, E.; Rakich, P.T.; Johnson, S.G.; Joannopoulos, J.D.; Ippen, E.P.; Smith, H.I. A three-dimensional optical photonic crystal with designed point defects. Nature **2004**, 429, 538–542.
 - 4. Joannopoulos, J.D.; Villeneuve, P.R.; Fan, S.H. Photonic crystals: Putting a new twist on light. Nature 1997, 386, 143–149.
 - Rinnerbauer, V.; et al. Superlattice photonic crystal as broadband solar absorber for high temperature operation. Opt. Express 2014, 22, A1895.
 - 6. Rinnerbauer, V.; et al. Nanoimprinted superlattice metallic photonic crystal as ultraselective solar absorber. Optica. **2015**, 2, 743.
 - 7. Lowell, D.; Lutkenhaus, J.; George, D.; Philipose, U.; Chen, B.; Lin, Y. Simultaneous direct holographic fabrication of photonic cavity and graded photonic lattice with dual periodicity, dual basis, and dual symmetry. Opt. Express 2017, 25, 14444.
 - 8. Hassan, S.; Lowell, D.; Lin, Y. High light extraction efficiency in organic light-emitting diodes by patterning the cathode in graded superlattice with dual periodicity and dual basis. J. Appl. Phys. **2017**, 121, 233104.
 - 9. Hassan, S.; Lowell, D.; Adewole, M.; George, D.; Zhang, H.; Lin, Y. Extraordinary light trapping enhancement in silicon solar cell patterned with graded photonic super-crystals. Photonics 2017, 4, 50.
 - Lowell, D.; Hassan, S.; Adewole, M.; Philipose, U.; Chen, B.; Lin, Y. Holographic fabrication of graded photonic super-crystals using an integrated spatial light modulator and reflective optical element laser projection system. Appl. Opt. 2017, 56, 9888.
 - 11. Lowell, D.; Hassan, S.; Sale, O.; Adewole, M.; Hurley, N.; Philipose, U.; Chen, B.; Lin, Y. Holographic fabrication of graded photonic super-quasi-crystal with multiple level gradients. Applied Optics **2018**, 57, 6598.
 - 12. Campbell, M.; Sharp, D.N.; Harrison, M.T.; Denning, R.G.; Turberfield, A.J. Fabrication of photonic crystals for the visible spectrum by holographic lithography. Nature **2000**, 404, 53–56.
 - 13. Lin, Y.; Herman, P.R.; Darmawikarta, J. Design and holographic fabrication of tetragonal and cubic photonic crystals with phase mask: Toward the mass-production of three-dimensional photonic crystals. Appl. Phys. Lett. **2005**, 86, 071117.

- Chanda, D.; Abolghasemi, L.E.; Haque, M.; Ng, M.L.; Herman, P.R. Multi-level diffractive optics for single laser exposure fabrication of telecom-band diamond-like 3-dimensional photonic crystals. Opt.
 Express 2008, 16, 15402–15414.
- 306 15. Ohlinger, K.; Zhang, H.; Lin, Y.; Xu, D.; Chen, K.P. A tunable three layer phase mask for single laser exposure 3D photonic crystal generations: Bandgap simulation and holographic fabrication. Opt. Mater. Express 2008, 1, 1034–1039.
 - Chan, T.Y.M.; Toader, O.; John, S. Photonic band-gap formation by optical-phase-mask lithography. Phys. Rev. E 2006, 73, 046610.
 - 17. Xu, D.; Chen, K.P.; Harb, A.; Rodriguez, D.; Lozano, K.; Lin, Y. Phase tunable holographic fabrication for three-dimensional photonic crystal templates by using a single optical element. Appl. Phys. Lett. **2009**, 94, 231116.
 - 18. George, D.; Lutkenhaus, J.; Lowell, D.; Moazzezi, M.; Adewole, M.; Philipose, U.; Zhang, H.; Poole, Z.L.; Chen, K.P.; Lin, Y. Holographic fabrication of 3D photonic crystals through interference of multibeams with 4 + 1, 5 + 1 and 6 + 1 configurations. Opt. Express **2014**, 22, 22421–22431.
 - 19. Lutkenhaus, J.; Farro, F.; George, D.; Ohlinger, K.; Zhang, H.; Poole, Z.; Chen, K.P.; Lin, Y. Holographic fabrication of 3D photonic crystals using silicon based reflective optics element. Opt. Mater. Express 2012, 2, 1236–1241.
 - 20. Xavier, J.; Boguslawski, M.; Rose, P.; Joseph, J.; Denz, C. Reconfigurable optically induced quasicrystallographic three-dimensional complex nonlinear photonic lattice structures. Adv. Mater. **2010**, 22, 356–360.
 - 21. Arrizón, V.; Sánchez-de-la-Llave, D.; Méndez, G.; Ruiz, U. Efficient generation of periodic and quasi-periodic non-diffractive optical fields with phase holograms. Opt. Express 2011, 34, 10553–10562.
 - 22. Boguslawski, M.; Rose, P.; Denz, C. Increasing the structural variety of discrete nondiffracting wave fields. Phys. Rev. A **2011**, 84, 013832.
 - 23. Behera, S.; Joseph, J. Single-step optical realization of bio-inspired dual-periodic motheye and gradient-index-array photonic structures. Opt. Lett. **2016**, 41, 3579.
 - 24. Lutkenhaus, J.; George, D.; Moazzezi, M.; Philipose, U.; Lin, Y. Digitally tunable holographic lithography using a spatial light modulator as a programmable phase mask. Opt. Express **2013**, 21, 26227-26235.
 - 25. Lutkenhaus, J.; George, D.; Arigong, B.; Zhang, H.; Philipose, U.; Lin, Y. Holographic fabrication of functionally graded photonic lattices through spatially specified phase patterns. Appl. Opt. **2014**, 53, 2548-2555.
 - Ohlinger, K.; Lutkenhaus, J.; Arigong, B.; Zhang, H.; Lin, Y. Spatially addressable design of gradient index structures through spatial light modulator based holographic lithography. J. Appl. Phys. 2013, 114, 213102.
 - 27. Lutkenhaus, J.; Lowell, D.; George, G.; Zhang, H.; Lin, Y. Holographic Fabrication of Designed Functional Defect Lines in Photonic Crystal Lattice Using a Spatial Light Modulator. Micromachines **2016**, 7, 59.
 - 28. Oskooi, A.F.; Roundy, D.; Ibanescu, M.; Bermel, P.; Joannopoulos, J.D.; and Johnson, S.G. MEEP: A flexible free-software package for electromagnetic simulations by the FDTD method. Comput. Phys. Commun. **2010**, 181, 687.
 - 29. Oskooi, A. Texturing the cathode of white organic light-emitting diodes with a lattice of nanoscale scatterers for enhanced light out-coupling. Appl. Phys. Lett. **2015**, 106, 041111.
 - 30. Grell, M.; and Bradley, D.D.C. Polarized luminescence from oriented molecular materials. Adv. Mater. 1999, 11, 895–905.
 - 31. Shi, J.; Pollard, M. E.; Angeles, C. A.; Chen, R.; Gates, J.C. M. D. B. Charlton Photonic crystal and quasi-crystals providing simultaneous light coupling and beam splitting within a low refractive-index slab waveguide. *Scientific Reports.* 2017, 7, 1812.
 - 32. Adewole, M.; Lowell, D.; Hassan, S.; George, D.; Zhang, H.; Cui J. and Lin, Y. Broadband Plasmonic Total Light Absorption in an Al-doped ZnO/spacer/silver Stack Patterned with Graded Photonic Super-crystal. Res. J. Opt. Photonics 2017, 1, 1-1.



© 2018 by the authors. Submitted for possible open access publication under the terms and conditions of the Creative Commons Attribution (CC BY) license (http://creativecommons.org/licenses/by/4.0/).